

Supporting Information:

On the interplay of solvent and conformational effects in simulated excited-state dynamics of a copper phenanthroline photosensitizer

Gianluca Levi,^{*,†} Elisa Biasin,[‡] Asmus O. Dohn,[†] and Hannes Jónsson[†]

[†]*Science Institute and Faculty of Physical Sciences, University of Iceland, 107 Reykjavík, Iceland*

[‡]*PULSE Institute, SLAC National Accelerator laboratory, Menlo Park, California 94025, USA*

E-mail: giale@hi.is

Contents

1	Molecular structure	S-2
2	Properties of the electronic excitation	S-3
3	Details of the fittings	S-8
4	Initial conditions for the S_1 QM/MM trajectories	S-10
5	Ground-state distribution of methyl dihedral angles	S-12
6	ASE implementation of an acetonitrile force field	S-12
7	Holonomic constraints for linear triatomic molecules	S-15
8	Cartesian coordinates of the optimized geometries	S-20
	References	S-23

1 Molecular structure

The geometries of $[\text{Cu}(\text{dmphen})_2]^+$ in the ground and S_1 excited states were fully optimized in vacuum with DFT at the same level of theory as in the QM/MM BOMD and NEB calculations presented in the main text. The minimum energy structure is found by employing the ASE implementation of a quasi-Newton local optimization algorithm using GPAW-computed forces. The geometry is converged when the magnitude of the maximum force of any atom is less than $0.02 \text{ eV}/\text{\AA}$. We find that the ground and excited states have approximate D_2 and C_2 symmetry, respectively. The cartesian coordinates of the optimized S_0 and S_1 geometries are reported in Table S3, section 8, while Table S1 reports selected structural parameters compared to the averages over equilibrated frames of the QM/MM trajectories.

Table S1: Selected structural parameters of the optimized gas-phase geometry of $[\text{Cu}(\text{dmphen})_2]^+$ in the S_0 and S_1 states, and corresponding average values from the QM/MM BOMD simulations at 300 K with their standard deviations. For the excited-state QM/MM averages, only equilibrated frames after 3 ps of the trajectory propagation were considered.

	S_0		S_1	
	Vacuum	QM/MM	Vacuum	QM/MM
bonds (\AA)				
$\langle \text{Cu-N} \rangle$	2.07	2.08 ± 0.03	2.02	2.05 ± 0.03
angles (deg.)				
$\langle \text{N-Cu-N} \rangle$	82.1	81.9 ± 1.8	84.2	83.2 ± 1.6
Θ (flattening)	86.9	88.6 ± 6.8	63.8	66.2 ± 5.5 (left) 113.4 ± 5.4 (right) ^a
Θ' (rocking) ^b	89.3	87.9 ± 6.1	89.5	88.9 ± 7.7

^a Left and right configurations correspond to a left- and right-handed twist of the ligands, respectively (see Figure S7). ^b The rocking angle is defined as the angle between the bisector of a N-Cu-N angle in one phenanthroline ligand and the normal to the N-Cu-N plane on the other ligand.^{S1}

Apart from the flattening distortion discussed in the main text, other significant structural changes in the S_1 state are a contraction of the Cu-N bonds and a widening of the N-Cu-N angles. These modifications are due to the removal of an electron from metal-centered d orbitals with some Cu-N antibonding character (see next section), and are consistent with experimental determinations.^{S2,S3} A transient X-ray absorption study by Chen *et al.*^{S4} deduced a significant rocking distortion in the excited state in solution following ligation of a solvent molecule to Cu to form a pentacoordinated exciplex. In the present study, exciplex formation is not observed. Accordingly, we find only a small rocking angle both in vacuum and in solution (see Table S1). This confirms what is observed by Penfold *et al.*^{S2} in a recent combined X-ray absorption and DFT investigation.

2 Properties of the electronic excitation

The $S_0 \rightarrow S_1$ vertical excitation energy computed using BLYP and the Δ SCF method in GPAW (see Computational Methods section in the main text) at the ground-state optimized

geometry of $[\text{Cu}(\text{dmphen})_2]^+$ in vacuum is 2.35 eV. This value differs from the position of the $S_0 \rightarrow S_1$ peak in the experimental absorption spectrum in solution, 2.25-2.29 eV,^{S2,S5,S6} by less than 4%. In comparison, the $S_0 \rightarrow S_1$ transition energy computed with linear response time-dependent (TD) DFT using the B3LYP hybrid functional and all-electron atomic orbital basis sets by Capano *et al.*^{S7} is 2.44 eV.

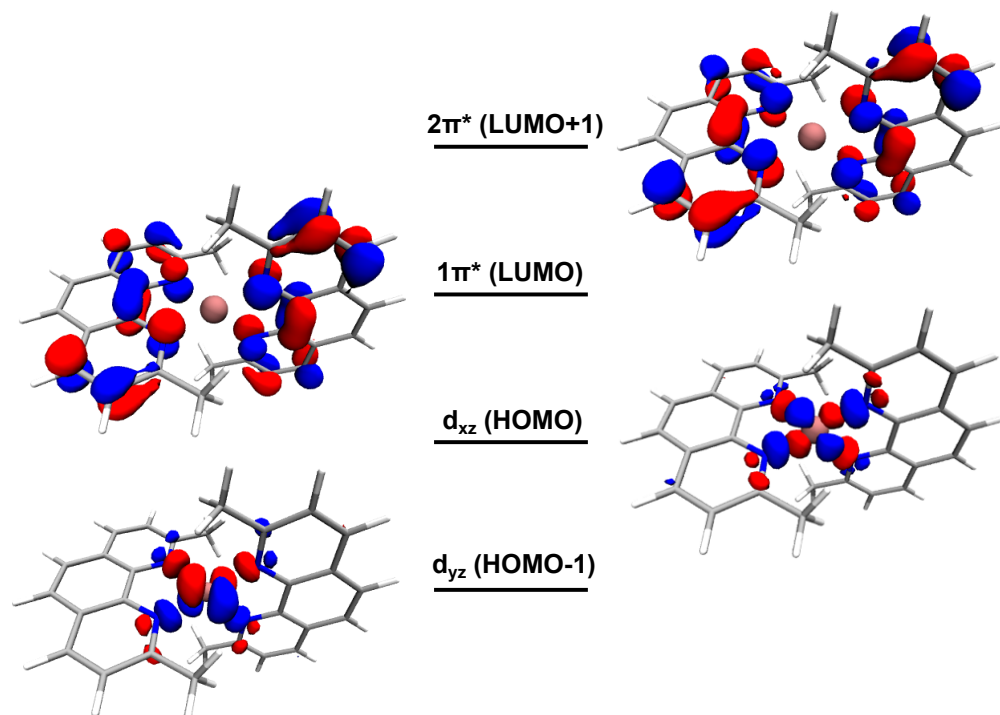


Figure S1: Molecular orbitals involved in the $S_0 \rightarrow S_1$ transition at the GPAW gas-phase optimized geometry of $[\text{Cu}(\text{dmphen})_2]^+$ in the ground state. Isovalues are at $0.1 \sqrt{e^-/\text{\AA}^3}$.

Figure S1 shows the molecular orbitals of $[\text{Cu}(\text{dmphen})_2]^+$ in the ground state involved in the electronic transition to S_1 . HOMO-1 and HOMO have character of d metal orbitals and are found to be almost degenerate at the gas-phase S_0 optimized geometry, while LUMO and LUMO+1 are ligand-centered π^* orbitals and they too are almost degenerate. Therefore, the $S_0 \rightarrow S_1$ excitation at the Franck-Condon (FC) geometry occurs from both HOMO-1 and HOMO to LUMO and LUMO+1, and displaces electron density from the metal to both phenanthroline ligands. The net charge transfer is $\sim 0.5 e^-$, as evaluated from the integral of the positive or negative parts of the electron density difference ($S_1 - S_0$, see Figure S2). As

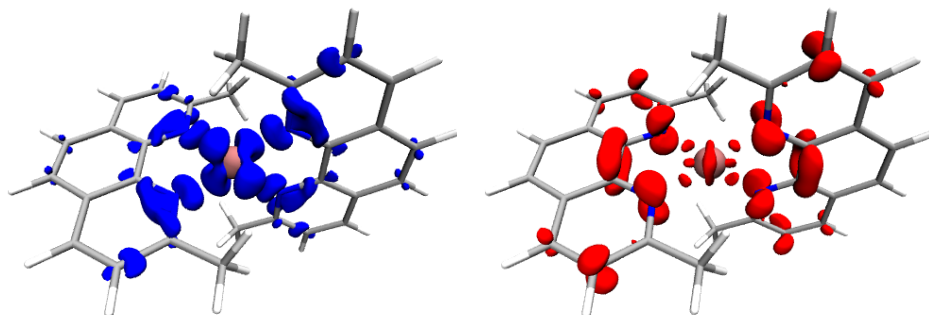


Figure S2: Negative (Left) and positive (Right) isovalues of the difference between the electron density of $[\text{Cu}(\text{dmphen})_2]^+$ ($S_1 - S_0$) at the GPAW gas-phase optimized geometry in the ground state. Isovalues are at $0.01 \text{ e}^-/\text{\AA}^3$.

the ligands flatten in the excited state, the orbital degeneracies are lifted and S_1 becomes characterized by a single transition, $d_{xz} \rightarrow 2\pi^*$ or $d_{yz} \rightarrow 1\pi^*$ depending on whether the twist of the ligands is left- or right-handed. A similar adiabatic picture of the lowest energy MLCT excitation has previously been obtained from B3LYP TDDFT calculations:^{S7-S10} In the perpendicular geometry, the S_1 state is characterized by a combination of $d \rightarrow \pi^*$ transitions, while at the excited-state minimum energy structure the transition occurs from a single d metal orbital to a single π^* ligand orbital. The major difference between the character of the S_1 state obtained from ΔSCF with BLYP and from TDDFT with B3LYP, is that for the former at the excited-state minimum the MLCT electron is delocalized on both phenanthroline ligands^{S8} while for the latter the photoexcited electron is localized on a single ligand.

To explore to which extent the character of the S_1 state is preserved in the nonequilibrium excited-state QM/MM BOMD simulations in acetonitrile, Figure S3 shows the evolution of the energy gap between the HOMO and LUMO (ground-state LUMO and LUMO+1) orbitals during the dynamics of a single QM/MM trajectory. At the beginning, the two orbitals are essentially degenerate and have both occupation numbers of ~ 0.5 , but after a fast relaxation time of around 400 fs, which parallels the pseudo Jahn-Teller (PJT) relaxation of the complex, the HOMO-LUMO gap fluctuates around an average of ~ 0.1 eV, preventing mixing of the HOMO with higher lying orbitals. This suggests that, after flattening, the

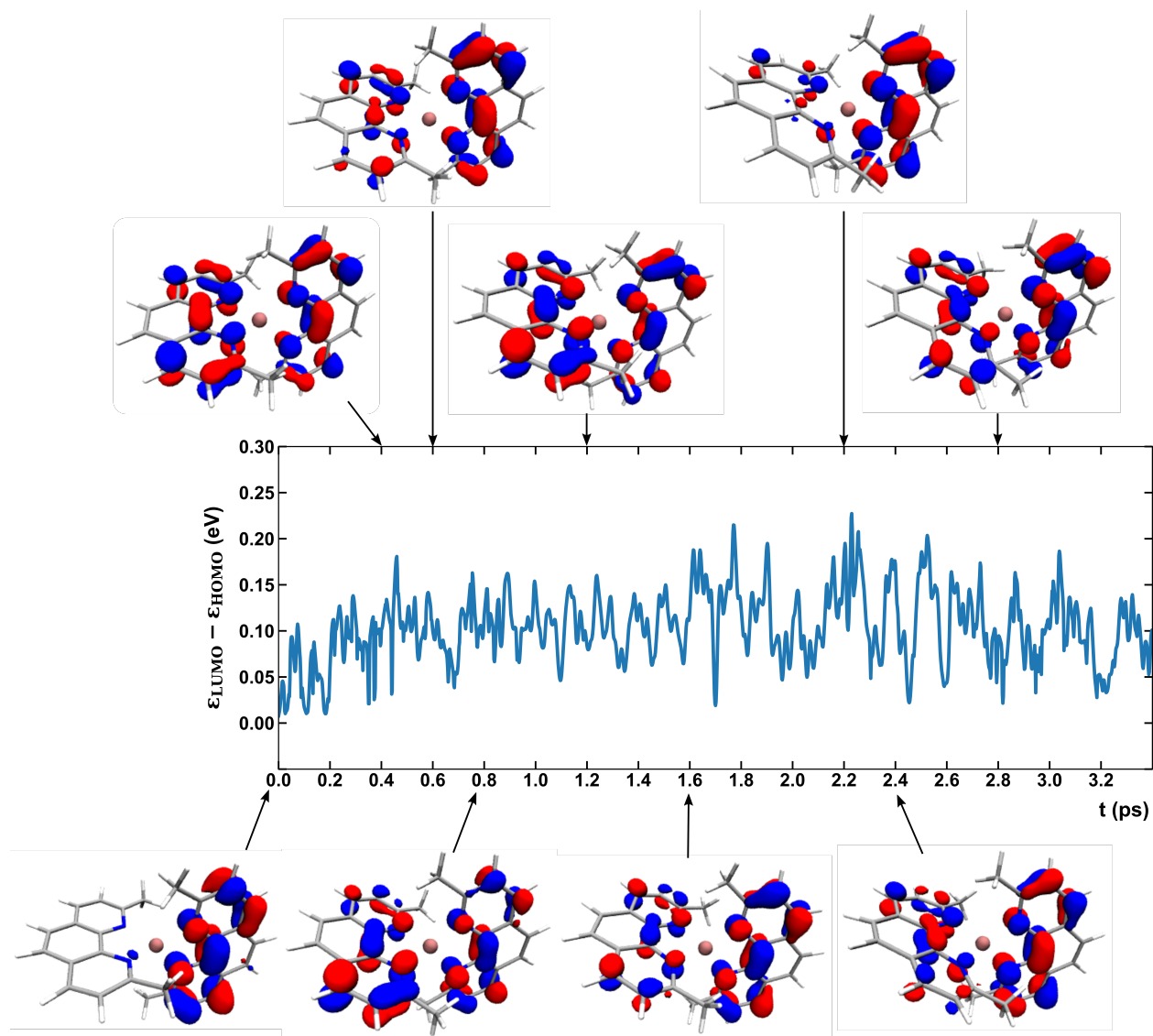


Figure S3: Time evolution of the HOMO-LUMO energy gap along a QM/MM trajectory of $[\text{Cu}(\text{dmphen})_2]^+$ in the S_1 state in acetonitrile. Above and below the plot, the HOMO orbital is depicted at the $0.01 \text{ e}^-/\text{\AA}^3$ isosurface at various times, as indicated by the arrows.

excited state to a large extent preserves a character of $d_{xz} \rightarrow 2\pi^*$ transition. A further indication of this is given by plots of an isosurface of the HOMO orbital at different times in the dynamics, also shown in Figure S3. The HOMO has a character of $2\pi^*$ orbital and is for most of the time delocalized over the two ligands. Localization of the π^* orbital on one ligand can occur sporadically, as for example at around 2.2 ps in the selected trajectory. Localization of the photoexcited electron for some instantaneous solvent configurations has

been observed in QM/MM simulations of the MLCT excited state of other transition metal compounds.^{S11}

Raman spectroscopic studies in solution^{S12} suggest that in the lowest ¹MLCT excited state (S_1) of $[\text{Cu}(\text{dmphen})_2]^+$ the promoted electron localizes on one phenanthroline ligand. To assess the extent to which the solvation structure is modified by the localization of the charge in the excited state, we perform additional classical MD simulations of $[\text{Cu}(\text{dmphen})_2]^+$ in acetonitrile, describing both solute and solvent at MM level. Acetonitrile molecules are modeled with the same classical force field as used in the QM/MM BOMD simulations (see section 6 below), while for the Coulombic interactions involving atoms of the solute we employ partial charges obtained from a Hirshfeld analysis^{S13} of the GPAW-calculated charge density of $[\text{Cu}(\text{dmphen})_2]^+$ in the ground or excited state in vacuum. The computed Hirshfeld partial charges, q_i^{gs} and q_i^{es} , are reported in Table S3, section 8. As expected, the negative charge transferred from the metal in the excited state is distributed uniformly among both ligands. Other nonbonded interactions are modeled with the Lennard-Jones (LJ) potential using parameters for the complex from the OPLS 2005 force field.^{S14} For these simulations, we use the Desmond software package developed at D. E. Shaw Research.^{S15} The complex is kept at the optimized ground- or excited-state gas-phase geometry by applying harmonic positional restraints with force constant of 500 kcal/mol, and solvated in a cubic box with 50 Å side length containing acetonitrile molecules. The propagation is performed in the NVT ensemble using a Nosé-Hoover thermostat at 300 K, with a time step of 2 fs for 500 ps, collecting frames every 500 fs. For the S_1 state, we perform two types of classical MD simulations, differing in the choice of partial charges for the ligands: (i) using for the atoms of the ligands partial charges q_i^{es} as calculated from the Hirshfeld analysis of the excited-state electron density and reported in Table S3 (charge delocalized uniformly on both ligands), and (ii) using for the atoms of one ligand the partial charges of the ground state (q_j^{gs} , where j is an index for the atoms of the first ligand) and for the atoms of the other ligand partial charges obtained as $q_k^{\text{gs}} + 2(q_k^{\text{es}} - q_k^{\text{gs}})$, where k is an index for the atoms

of the second ligand (transferred charge localized on one ligand).

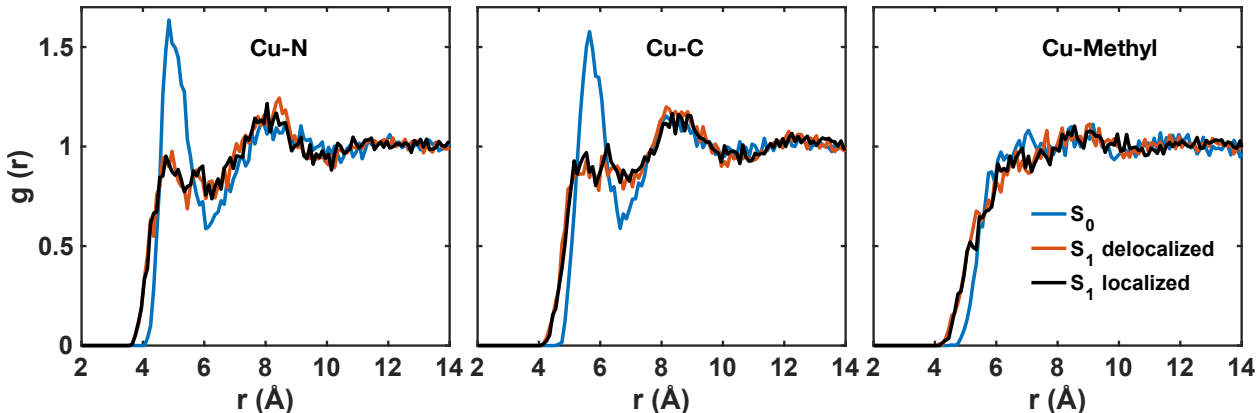


Figure S4: RDFs between Cu and the sites of the acetonitrile molecules as obtained from MM MD simulations of $[\text{Cu}(\text{dmphen})_2]^+$ in the ground state and in the excited state with different distributions of the transferred charge among the two phenanthroline ligands. The RDFs from the MM trajectories appear more structured than those computed from the QM/MM trajectories (see Figure 3 in the main text), a feature that can be in part ascribed to the rigidity of the solute in the MM MD simulations.^{S16}

Figure S4 shows the Cu-solvent pairwise radial distribution functions (RDFs) obtained from the frames collected from the MM MD trajectories by sampling the atom pairs in 0.1 Å radial bins. There are no sizable differences between the RDFs for the two different types of localization of the extra negative charge on the ligands in the excited state of $[\text{Cu}(\text{dmphen})_2]^+$, apart from noise due to the limited sampling statistics. Thus, the response of the solvent to MLCT excitation of the complex is the same whether the charge is transferred to one or both of the ligands.

3 Details of the fittings

The exponential functions fitted to the time evolution of the average deviation from 90° of the flattening angle Θ , as extracted from the excited-state QM/MM and gas-phase BOMD simulations, and to the instantaneous cumulative coordination number obtained by integrating

the Cu-N(solvent) RDFs up to $r(\text{Cu} - \text{N}) = 4.75 \text{ \AA}$, have the general form:

$$f(t) = \sum_i A_i e^{-t/\tau_i} + B \quad (1)$$

Table S2 reports the parameters for each of the best fits presented in the main text.

Table S2: Parameters of the exponential fits shown in Figures 2-4 of the main text. Θ is the dihedral angle defined in Figure 1, $\langle \dots \rangle$ indicates averages over trajectories, and cn is the cumulative coordination number of the distances between Cu and the N sites of the acetonitrile molecules at $r(\text{Cu} - \text{N}) = 4.75 \text{ \AA}$ obtained from the S_1 QM/MM trajectories.

	$\langle 90^\circ - \Theta \rangle$ solution		cn	$\langle 90^\circ - \Theta \rangle$ vacuum
	Monoexponential	Biexponential		
A_1	$-12.6 \pm 0.4 \text{ deg.}$	$-11.3 \pm 0.6 \text{ deg.}$	-0.77 ± 0.01	$-16 \pm 2 \text{ deg.}$
A_2	-	$-5.3 \pm 0.4 \text{ deg.}$	-	-
τ_1	$300 \pm 14 \text{ fs}$	$110 \pm 12 \text{ fs}$	$1060 \pm 49 \text{ fs}$	$90 \pm 16 \text{ fs}$
τ_2	-	$1200 \pm 190 \text{ fs}$	-	-
B	$21.8 \pm 0.1 \text{ deg.}$	$22.7 \pm 0.2 \text{ deg.}$	1.29 ± 0.01	$20.0 \pm 0.2 \text{ deg.}$
R^2	0.78	0.86	0.87	0.19

Figure S5 shows the residuals of a fit of the instantaneous deviation from 90° of the flattening angle Θ averaged over the excited-state QM/MM trajectories with a monoexponential and a biexponential function, respectively. The oscillations with a period of $\sim 140 \text{ fs}$ are due to a vibrational mode with character of twisting of the ligands, which is activated at the beginning of the excited-state dynamics and involves a bending of the Θ angle, as confirmed by a normal mode analysis at the gas-phase S_1 optimized geometry. For a better comparison of the quality of the monoexponential and biexponential fits, the residuals are averaged over bins of 140 fs and plotted in Figure S6.

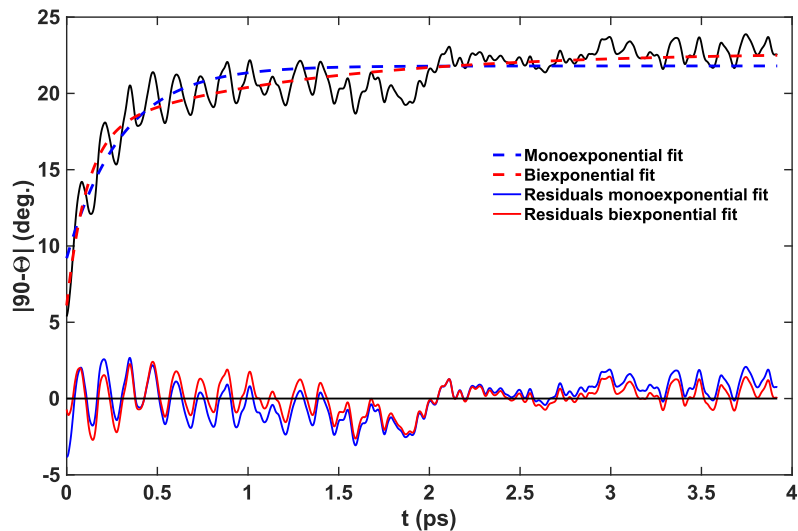


Figure S5: Evolution of the average flattening angle Θ (see Figure 1 in the main text for a definition of Θ) from the nonequilibrium excited-state QM/MM simulations of $[\text{Cu}(\text{dmphen})_2]^+$ in acetonitrile (black curve), together with monoexponential and biexponential fits, and their respective residuals (average $|90^\circ - \Theta|$ minus fitted curves). The instantaneous average of $|90^\circ - \Theta|$ and the fitted curves are already shown in Figure 2 of the main text.

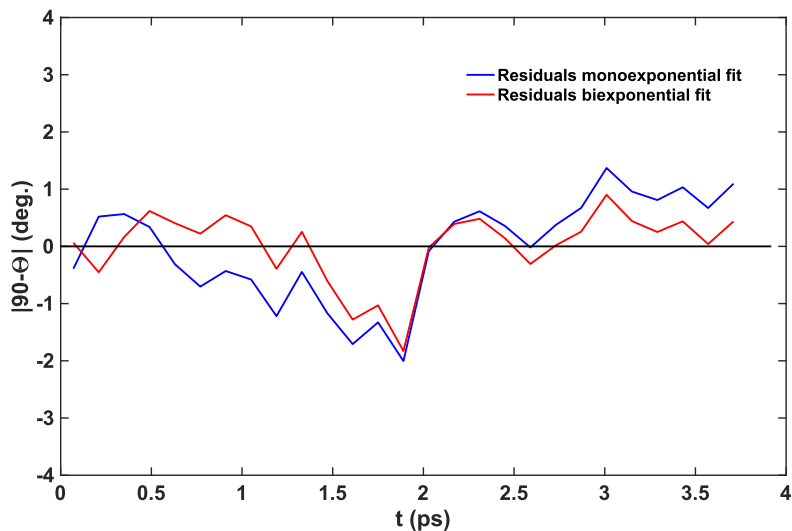


Figure S6: Residuals of monoexponential and biexponential fits to the instantaneous $|90^\circ - \Theta|$ from the nonequilibrium excited-state QM/MM simulations averaged over time bins of 140 fs.

4 Initial conditions for the S_1 QM/MM trajectories

Photoexcitation of ground-state $[\text{Cu}(\text{dmphen})_2]^+$ molecules from a thermal equilibrium ensemble to the S_1 state is assumed to be an instantaneous process. Figure S7 illustrates how

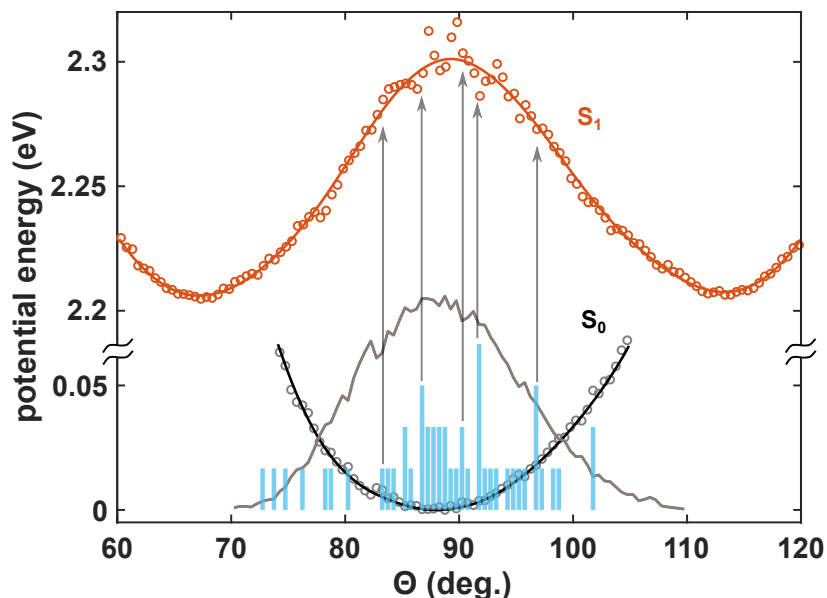


Figure S7: Schematic representation of the generation of initial conditions for the propagation of the nonequilibrium BOMD trajectories of $[\text{Cu}(\text{dmphen})_2]^+$ in the S_1 state in acetonitrile or vacuum. The black and red dots are free energy curves obtained as potential of mean force (PMF) using the distributions of flattening angles Θ built from the equilibrated ground-state QM/MM BOMD data (grey curve) and from *all* S_1 QM/MM BOMD data (not shown), respectively; while the continuous black and red curves are cubic spline fits. Histogramming the Θ values of the ground-state QM/MM frames selected for the excited-state propagation gives the (unnormalized) distribution shown with blue vertical bars. The vertical arrows depict the promotion of ground-state molecules to S_1 .

nonequilibrium initial conditions for the propagation of the excited-state QM/MM and gas-phase trajectories are generated according to this picture of instantaneous excitation. First, data from the QM/MM BOMD simulations in the canonical ensemble at 300 K (around 65000 frames forming a statistically significant classical distribution of configurations in thermal equilibrium with the solvent) are collected. Subsequently, 48 S_1 (QM/MM as well as gas-phase) trajectories are started using initial positions and velocities from QM/MM frames drawn randomly from this ground-state equilibrium ensemble. Due to the flexibility along the flattening coordinate in the ground state at 300 K, molecules that can be excited possess a wide range of flattening angles Θ , as implied from the histogram of selected configurations shown in Figure S7.

5 Ground-state distribution of methyl dihedral angles

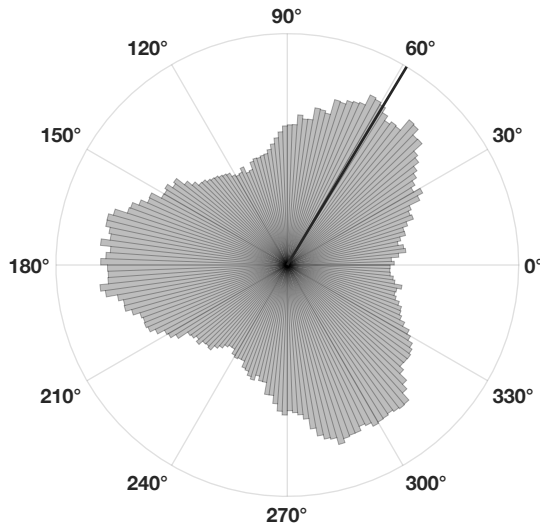


Figure S8: Polar distribution of HCCN methyl dihedral angles Γ in $[\text{Cu}(\text{dmphen})_2]^+$ (see Figure 5 in the main text) sampled from the 300 K equilibrated QM/MM BOMD data of the complex in the ground-state. The black line represents the average of the distribution considering the peak at low angles.

6 ASE implementation of an acetonitrile force field

The QM/MM BOMD simulations performed in this work use a classical force field for acetonitrile. We opted for the pairwise interaction potential from Guàrdia *et al.*,^{S17} which was shown to deliver structural and thermodynamic properties for liquid acetonitrile in fairly good agreement with experiments. Acetonitrile is modeled as a linear molecule with three interaction sites, corresponding to the Nitrogen atom, the middle Carbon and the methyl group (Me), respectively. The bond lengths are $d_{\text{MeC}} = 1.458 \text{ \AA}$ and $d_{\text{CN}} = 1.157 \text{ \AA}$. The form of the interaction energy between two acetonitrile molecules, acn1 and acn2, is the following:

$$E_{\text{acn1-acn2}} = \sum_{i \in \text{acn1}} \sum_{j \in \text{acn2}} \left\{ \frac{q_i q_j}{r_{ij}} + 4\epsilon_{ij} \left[\left(\frac{\sigma_{ij}}{r_{ij}} \right)^{12} - \left(\frac{\sigma_{ij}}{r_{ij}} \right)^6 \right] \right\} \quad (2)$$

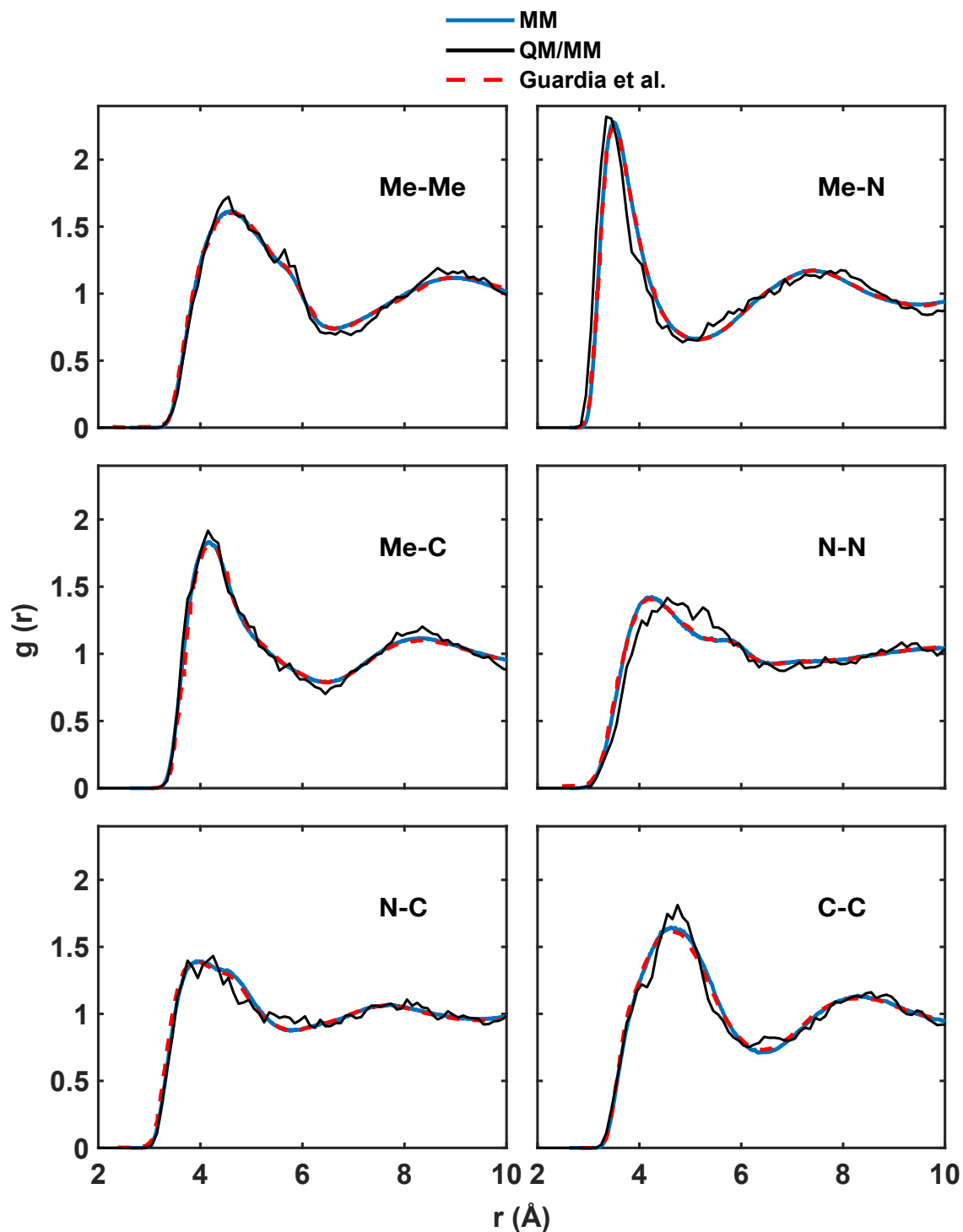


Figure S9: RDFs between sites of acetonitrile molecules simulated by full MM MD and QM/MM BOMD at 300 K using the implementation of a classical pairwise potential for acetonitrile in ASE. The QM/MM RDFs are computed between the atoms of a single QM acetonitrile and the sites the MM molecules. The agreement with the RDFs presented by Guàrdia *et al.*,^{S17} who first proposed this classical force field for acetonitrile, confirms the ASE implementation has been carried out correctly.

where r_{ij} is the distance between site i on molecule acn1 and site j on molecule acn2, q_i and q_j their partial charges, and ϵ_{ij} and σ_{ij} are Lennard-Jones (LJ) parameters. The interaction parameters were determined by Guàrdia *et al.*^{S17} by fitting *ab initio* calculations of the acetonitrile dimer in different configurations.

We have implemented this classical interaction potential for acetonitrile in the ASE program, in conjunction with a method for holonomic constraints for rigid linear triatomic systems (see following section). We validate the implementation by simulating 494 MM acetonitrile molecules in a cubic box with 35 Å side length (giving the density of acetonitrile at ~ 300 K) by MD in the NVT ensemble. The box was first equilibrated at 300 K, after which propagation was continued for around 100 ps with a time step of 1 fs. In this simulation, thermal equilibrium is achieved using the Langevin thermostat implemented in ASE, while periodic boundary conditions are treated according to the minimum image convention. Figure S9 shows the RDFs for all atomic pairs sampled from the equilibrated trajectory with a radial bin of 0.01 Å. There is a very good correspondence between these RDFs and those reported by Guàrdia *et al.*^{S17} from MD simulations at a constant temperature of 298 K using the same acetonitrile force field (also shown in Figure S9).

We further test the QM/MM electrostatic embedding interfacing between the acetonitrile classical potential in ASE and the GPAW DFT code by propagating a BOMD trajectory of a single QM acetonitrile molecule in MM acetonitrile at the density of the liquid at 300 K, as in the full MM simulation. The QM subsystem is described using the PBE functional and tzp basis set^{S18} in a GPAW cell with 0.18 Å grid spacing. We choose to use the same LJ parameters for the QM and MM molecules, with the exception of the Hydrogen atoms of the QM acetonitrile, which are excluded from the computation of LJ interactions. The propagation is done in the NVT ensemble at 300 K with a 1 fs time step for ~ 75 ps after thermal equilibration. During the dynamics, all C-H bond lengths and H-H distances within the QM molecule are constrained with the ASE implementation of RATTLE.^{S19} Figure S9 compares the RDFs sampled from the atoms of the single QM acetonitrile (excluding the H

atoms) to the sites of the MM molecules with the MM RDFs. The good agreement between the MM and QM/MM descriptions confirms the reliability of the QM/MM interfacing.

7 Holonomic constraints for linear triatomic molecules

Molecular dynamics simulations of rigid molecular systems are most often performed by applying bond constraints between pairs of particles in cartesian coordinates.^{S20,S21} In certain cases, however, bond constraints alone cannot ensure rigidity of the molecular geometry,^{S22,S23} and special handling is required. One example is represented by linear triatomic molecules, since defining bond constraints between the atomic pairs does not remove all four internal degrees of freedom. In order to employ the three-site acetonitrile force field from Guàrdia *et al.*^{S17} presented in the previous section in MD simulations, we have implemented a scheme for holonomic constraints adapted from Ciccotti *et al.*^{S23} The implementation is available within the ASE program and can be used to perform MD simulations of any kind of rigid linear triatomic system in cartesian coordinates in the NVE and NVT ensembles.

Let us consider a triatomic molecular entity A-C-B. The implemented strategy applies a bond constraint σ to fix the distance d_{AB} between the outer particles:

$$\sigma \equiv |\mathbf{r}_A - \mathbf{r}_B|^2 - d_{AB}^2 = 0 \tag{3}$$

and a linear vectorial constraint $\boldsymbol{\tau}$ connecting the position of the central particle C with those of A and B:

$$\boldsymbol{\tau} \equiv c_A \mathbf{r}_A + c_B \mathbf{r}_B - \mathbf{r}_C = 0 \tag{4}$$

where \mathbf{r}_i denotes position vectors in cartesian coordinates, and the constants c_A and c_B are determined from the fixed interparticle distances ($c_A = \frac{d_{CB}}{d_{AB}}$, $c_B = \frac{d_{AC}}{d_{AB}}$). The total forces on

the three particles are given by:

$$\mathbf{F}'_A = \mathbf{F}_A - \lambda \frac{\partial \sigma}{\partial \mathbf{r}_A} - \frac{\partial(\boldsymbol{\mu} \cdot \boldsymbol{\tau})}{\partial \mathbf{r}_A} = \mathbf{F}_A - 2\lambda \mathbf{r}_{AB} - c_A \boldsymbol{\mu} \quad (5a)$$

$$\mathbf{F}'_B = \mathbf{F}_B - \lambda \frac{\partial \sigma}{\partial \mathbf{r}_B} - \frac{\partial(\boldsymbol{\mu} \cdot \boldsymbol{\tau})}{\partial \mathbf{r}_B} = \mathbf{F}_B + 2\lambda \mathbf{r}_{AB} - c_B \boldsymbol{\mu} \quad (5b)$$

$$\mathbf{F}'_C = \mathbf{F}_C - \frac{\partial(\boldsymbol{\mu} \cdot \boldsymbol{\tau})}{\partial \mathbf{r}_C} = \mathbf{F}_C + \boldsymbol{\mu} \quad (5c)$$

where \mathbf{F}_A , \mathbf{F}_B and \mathbf{F}_C are the forces due to intramolecular and intermolecular potentials, λ and $\boldsymbol{\mu}$ are Lagrange multipliers associated with the constraints σ and $\boldsymbol{\tau}$ respectively, and we have used the abbreviated notation $\mathbf{r}_{AB} = \mathbf{r}_A - \mathbf{r}_B$. To propagate such a rigid system in an MD simulation, one only needs to explicitly integrate the equations of motion for the particles A and B, connected by a bond constraint, since the time evolution of the coordinates of C follows directly from the constraint $\boldsymbol{\tau}$ (Equation 4). In order to do that, an expression of $\boldsymbol{\mu}$ in terms of the atomic forces (\mathbf{F}_A , \mathbf{F}_B and \mathbf{F}_C) and λ needs to be found. This corresponds to a redistribution of the forces within the molecular system, and can be done by first writing the equations of motion for all three particles:

$$\ddot{\mathbf{r}}_A = \frac{1}{m_A} (\mathbf{F}_A - 2\lambda \mathbf{r}_{AB} - c_A \boldsymbol{\mu}) \quad (6a)$$

$$\ddot{\mathbf{r}}_B = \frac{1}{m_B} (\mathbf{F}_B + 2\lambda \mathbf{r}_{AB} - c_B \boldsymbol{\mu}) \quad (6b)$$

$$\ddot{\mathbf{r}}_C = \frac{1}{m_C} (\mathbf{F}_C + \boldsymbol{\mu}) \quad (6c)$$

where m_i are the masses; and then substituting these expressions in the second time derivative of the constraint $\boldsymbol{\tau}$ ($c_A \ddot{\mathbf{r}}_A + c_B \ddot{\mathbf{r}}_B - \ddot{\mathbf{r}}_C = 0$). By doing so, one obtains:

$$\boldsymbol{\mu} = \frac{1}{h} [m_B m_C c_A \mathbf{F}_A + m_A m_C c_B \mathbf{F}_B - m_A m_B \mathbf{F}_C - 2m_C (m_B c_A - m_A c_B) \lambda \mathbf{r}_{AB}] \quad (7)$$

with $h = m_B m_C c_A^2 + m_A m_C c_B^2 + m_A m_B$. The equations of motion for the particles A and B

are derived by inserting Equation 7 into Equations 6a and 6b:

$$\begin{aligned} m_A \ddot{\mathbf{r}}_A &= \left(1 - \frac{m_B m_C c_A^2}{h}\right) \mathbf{F}_A - \frac{m_A m_C c_A c_B}{h} \mathbf{F}_B + \frac{m_A m_B c_A}{h} \mathbf{F}_C - 2l_A \lambda \mathbf{r}_{AB} \\ &= \tilde{\mathbf{F}}_A - 2l_A \lambda \mathbf{r}_{AB} \end{aligned} \quad (8a)$$

$$\begin{aligned} m_B \ddot{\mathbf{r}}_B &= \left(1 - \frac{m_A m_C c_B^2}{h}\right) \mathbf{F}_B - \frac{m_B m_C c_A c_B}{h} \mathbf{F}_A + \frac{m_A m_B c_B}{h} \mathbf{F}_C + 2l_B \lambda \mathbf{r}_{AB} \\ &= \tilde{\mathbf{F}}_B + 2l_B \lambda \mathbf{r}_{AB} \end{aligned} \quad (8b)$$

where $l_A = -\frac{m_B m_C c_A^2 - m_A m_C c_A c_B - h}{h}$ and $l_B = -\frac{m_A m_C c_B^2 + m_B m_C c_A c_B - h}{h}$. The second equalities in Equations 8a and 8b define collective forces $\tilde{\mathbf{F}}_A$ and $\tilde{\mathbf{F}}_B$ acting on the outer particles. Clearly, the problem of propagating a rigid linear triatomic system is reduced to solving the equations of motion of a rigid diatomic molecule A-B with a particular redistribution of the forces. Once the time evolution of \mathbf{r}_A and \mathbf{r}_B is known from the integration of Equations 8a and 8b, the time-dependent \mathbf{r}_C is obtained from Equation 4:

$$\mathbf{r}_C = c_A \mathbf{r}_A + c_B \mathbf{r}_B \quad (9)$$

In ASE, the Velocity Verlet algorithm can be used to integrate the equations of motion for simulations in the NVE ensemble; while for NVT simulations, a second-order integrator of the Langevin equations^{S24} is available. In the following, we show how Equations 8a and 8b are integrated numerically using the Velocity Verlet algorithm.^{S19} The Velocity Verlet equations for propagation of the rigid unit A-B with a time step Δt can be written as:

$$\mathbf{r}_A(t + \Delta t) = \mathbf{r}'_A(t + \Delta t) - \frac{\Delta t^2}{m_A} l_A \lambda_p \mathbf{r}_{AB}(t) \quad (10a)$$

$$\dot{\mathbf{r}}_A(t + \Delta t) = \dot{\mathbf{r}}'_A(t + \Delta t) - \frac{\Delta t}{m_A} l_A [\Delta t \lambda_p \mathbf{r}_{AB}(t) + \lambda_v \mathbf{r}_{AB}(t + \Delta t)] \quad (10b)$$

$$\mathbf{r}_B(t + \Delta t) = \mathbf{r}'_B(t + \Delta t) + \frac{\Delta t^2}{m_B} l_B \lambda_p \mathbf{r}_{AB}(t) \quad (10c)$$

$$\dot{\mathbf{r}}_B(t + \Delta t) = \dot{\mathbf{r}}'_B(t + \Delta t) + \frac{\Delta t}{m_B} l_B [\Delta t \lambda_p \mathbf{r}_{AB}(t) + \lambda_v \mathbf{r}_{AB}(t + \Delta t)] \quad (10d)$$

where:

$$\mathbf{r}'_i(t + \Delta t) = \mathbf{r}_i(t) + \dot{\mathbf{r}}_i(t)\Delta t + \frac{\Delta t^2}{2m_i}\tilde{\mathbf{F}}_i(t) \quad (11a)$$

$$\dot{\mathbf{r}}'_i(t + \Delta t) = \dot{\mathbf{r}}_i(t) + \frac{\Delta t}{2m_i}\left[\tilde{\mathbf{F}}_i(t) + \tilde{\mathbf{F}}_i(t + \Delta t)\right] \quad (11b)$$

are the positions and velocities updated at time $t + \Delta t$ considering only forces that arise from intramolecular and intermolecular potentials. In Equations 10a-10d we have introduced different Lagrange multipliers, λ_p and λ_v , to correct positions and velocities for the forces due to the bond constraint. λ_p is determined such to satisfy the constraint σ (Equation 3) at time $t + \Delta t$, which is:

$$|\mathbf{r}_A(t + \Delta t) - \mathbf{r}_B(t + \Delta t)|^2 = d_{AB}^2 \quad (12)$$

This is done by inserting the right-hand side of Equations 10a and 10c in Equation 12, finding the above quadratic expression for λ_p :

$$\lambda_p = \frac{[\mathbf{r}'_{AB}(t + \Delta t) \cdot \mathbf{r}_{AB}(t)] - \sqrt{[\mathbf{r}'_{AB}(t + \Delta t) \cdot \mathbf{r}_{AB}(t)]^2 - \mathbf{r}_{AB}^2(t) [\mathbf{r}'_{AB}(t + \Delta t) - d_{AB}^2]}}{\Delta t \left(\frac{l_A}{m_A} + \frac{l_B}{m_B} \right) \mathbf{r}_{AB}^2(t)} \quad (13)$$

where l_A and l_B have been defined previously (see Equations 8a and 8b). The Lagrange multiplier for the correction of the velocities, λ_v , is chosen in order to satisfy the time derivative of the constraint in Equation 12:

$$[\dot{\mathbf{r}}_A(t + \Delta t) - \dot{\mathbf{r}}_B(t + \Delta t)] \cdot [\mathbf{r}_A(t + \Delta t) - \mathbf{r}_B(t + \Delta t)] = 0 \quad (14)$$

By using Equations 10b and 10d in Equation 14, the following expression for λ_v is obtained:

$$\lambda_v = \frac{\left[\dot{\mathbf{r}}'_A(t + \Delta t) - \dot{\mathbf{r}}'_B(t + \Delta t) - \Delta t^2 \left(\frac{l_A}{m_A} + \frac{l_B}{m_B} \right) \lambda_p \mathbf{r}_{AB}(t) \right] \cdot \mathbf{r}_{AB}(t + \Delta t)}{\left(\frac{l_A}{m_A} + \frac{l_B}{m_B} \right) d_{AB}^2} \quad (15)$$

Having derived expressions for the Lagrange multipliers associated with the bond constraint σ , it is possible to know the positions and velocities of the outer particles A and B of the rigid triatomic system at each subsequent time step through Equations 10a-10d. The positions and velocities of the central particle C follow directly from Equation 9. Figure S10 depicts a schematic summary of a step in the MD propagation of a rigid linear triatomic system with the presented method of holonomic constraints.

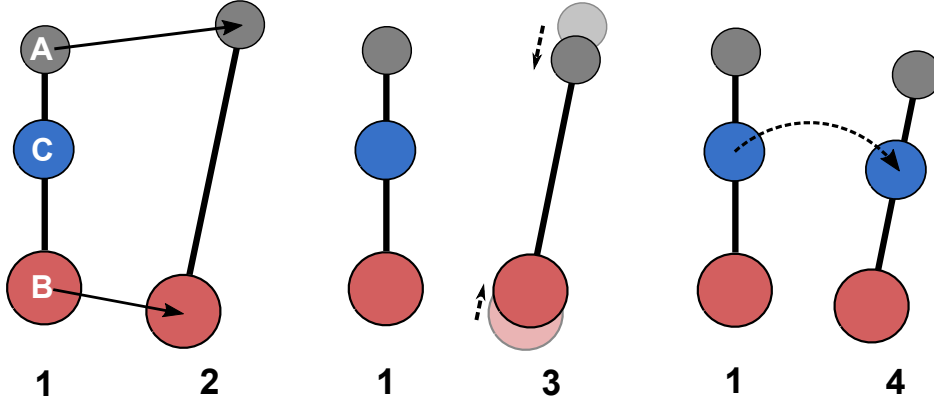


Figure S10: Schematic representation of the application of holonomic constraints in the MD propagation of a rigid linear triatomic system. Continuous arrows represent atomic displacements after an unconstrained MD step, while dashed arrows represent the adjustment of positions due to the constraints. **1** is the initial configuration, **2** is the configuration after unconstrained propagation of the diatomic unit A-B, **3** shows the application of the bond constraint (Equation 3), and **4** is the final configuration, with same internal geometry as **1**, after application of the linear vectorial constraint (Equation 4) to the position of C.

The constraint strategy described therein is readily extended to Velocity Verlet algorithms generalized for solving the Langevin equations of motion, like the second-order NVT integrator implemented in ASE,^{S24} provided that the additional stochastic forces are properly redistributed within the triatomic system as in Equations 8a and 8b. We further note

that in the presented scheme of holonomic constraints, Lagrange multipliers are efficiently computed noniteratively and without neglecting second order terms. This would not be possible if more than one bond constraint per triatomic system were present, in which case the iterative RATTLE algorithm^{S19} is required, thus increasing the computational cost of computing the Lagrange multipliers.

8 Cartesian coordinates of the optimized geometries

Table S3: Cartesian coordinates in Å and Hirshfeld partial charges in elementary charge unit for the gas-phase optimized structure of $[\text{Cu}(\text{dmphen})_2]^+$ in the S_0 and S_1 states

	S_0				S_1			
Atom	x	y	z	q^{gs}	x	y	z	q^{es}
Cu	12.19787	9.23250	9.22780	0.145	12.18337	10.09750	9.26471	0.273
N	10.64024	10.27301	8.35697	-0.107	10.68682	11.34390	8.74811	-0.111
N	10.64061	8.21928	10.13238	-0.107	10.68615	8.85342	9.79916	-0.111
C	8.22685	11.42441	7.39360	0.003	8.28080	12.67772	8.03901	-0.004
C	8.22792	7.07185	11.10059	0.003	8.27913	7.52266	10.51099	-0.003
C	9.40976	9.79885	8.77499	0.048	9.44190	10.75285	8.98681	0.036
C	9.41005	8.69532	9.71659	0.048	9.44147	9.44678	9.56395	0.036
C	10.67318	11.30736	7.47059	0.089	10.73548	12.55199	8.10240	0.088
C	10.67415	7.18751	11.02169	0.089	10.73464	7.64602	10.44580	0.088
C	8.16369	10.34156	8.31844	0.015	8.20332	11.40407	8.66236	0.015
C	8.16430	8.15427	10.17517	0.015	8.20255	8.79631	9.88817	0.015
C	9.47298	11.89903	6.97806	-0.022	9.54222	13.22816	7.74146	-0.031
C	9.47403	6.59690	11.51594	-0.022	9.54045	6.97181	10.80802	-0.031
C	6.92213	9.77536	8.80171	-0.014	6.96379	10.72287	8.97563	-0.012
C	6.92258	8.72045	9.69199	-0.014	6.96317	9.47836	9.57570	-0.012
H	9.54511	5.76279	12.23620	0.051	9.61655	5.99995	11.32588	0.049

H	7.29434	6.62030	11.48478	0.055	7.35345	6.97890	10.77542	0.054
H	5.97067	8.29046	10.05383	0.050	6.00909	8.97935	9.82711	0.051
H	5.97003	10.20493	8.43980	0.050	6.00983	11.22269	8.72428	0.051
H	7.29317	11.87666	7.01052	0.055	7.35593	13.22122	7.77224	0.054
H	9.54396	12.73446	6.25930	0.051	9.61989	14.20001	7.22336	0.049
C	12.03556	11.79764	7.02514	-0.071	12.09320	13.13812	7.76877	-0.070
H	12.62649	12.16835	7.89294	0.036	12.60943	13.53379	8.67194	0.036
H	12.62107	10.96750	6.56968	0.036	12.75788	12.36393	7.32618	0.033
H	11.94730	12.61732	6.28268	0.045	11.98883	13.97195	7.04437	0.048
C	12.03639	6.69577	11.46683	-0.071	12.09132	7.05574	10.77759	-0.070
H	12.62720	6.32519	10.59887	0.036	12.60112	6.65546	9.87287	0.036
H	12.62309	7.52430	11.92377	0.036	12.76121	7.82720	11.21798	0.033
H	11.94689	5.87530	12.20837	0.045	11.98374	6.22233	11.50226	0.048
N	13.75928	10.19110	10.22502	-0.108	13.68202	11.12325	10.16229	-0.111
N	13.75794	8.30508	8.27012	-0.106	13.68147	9.07847	8.38930	-0.111
C	16.18112	11.26367	11.26757	0.003	16.09161	12.13526	11.27892	-0.003
C	16.17183	7.22757	7.22404	0.002	16.08414	8.06404	7.27006	-0.004
C	14.99005	9.75436	9.76522	0.048	14.92519	10.62840	9.75640	0.036
C	14.98950	8.73924	8.73022	0.048	14.92491	9.57262	8.79488	0.036
C	13.73460	11.15583	11.18819	0.090	13.63622	12.06522	11.15791	0.088
C	13.72616	7.34085	7.30701	0.089	13.62957	8.13981	7.39118	0.087
C	16.23869	10.25719	10.26042	0.015	16.16542	11.13211	10.27692	0.015
C	16.23533	8.23393	8.23147	0.015	16.16304	9.06656	8.27232	0.015
C	14.93759	11.70666	11.72102	-0.022	14.83132	12.57364	11.72758	-0.031
C	14.92602	6.78600	6.77352	-0.022	14.82181	7.62816	6.82132	-0.031
C	17.47887	9.73306	9.73172	-0.014	17.40484	10.58708	9.76193	-0.012
C	17.47724	8.75662	8.75754	-0.014	17.40380	9.60963	8.78627	-0.012
H	18.43218	10.13114	10.12539	0.050	18.35830	10.97620	10.16382	0.051
H	18.42913	8.35742	8.36155	0.050	18.35663	9.21998	8.38390	0.051

H	17.10491	6.80454	6.80759	0.055	17.00868	7.63748	6.83928	0.054
H	14.85573	6.00582	5.99513	0.051	14.74287	6.87177	6.02148	0.049
H	14.87055	12.48657	12.50013	0.051	14.75344	13.33233	12.52559	0.049
H	17.11671	11.68427	11.68119	0.056	17.01743	12.55936	11.70877	0.054
C	12.36488	6.87869	6.82702	-0.071	12.27124	7.67376	6.90222	-0.070
H	11.77379	6.44711	7.66598	0.035	11.74279	7.06234	7.66720	0.035
H	11.77719	7.73568	6.42762	0.036	11.61539	8.54273	6.67146	0.034
H	12.45871	6.11080	6.03135	0.045	12.37812	7.05845	5.98534	0.048
C	12.37984	11.62820	11.67760	-0.070	12.28252	12.54431	11.64859	-0.070
H	11.78685	12.06460	10.84221	0.036	11.75995	13.16265	10.88463	0.035
H	11.78839	10.77525	12.08024	0.037	11.61774	11.68164	11.87742	0.035
H	12.48291	12.39454	12.47350	0.045	12.39629	13.15685	12.56630	0.048

References

- (S1) Dobson, J. F.; Green, B. E.; Healy, P. C.; Kennard, C. H. L.; Pakawatchai, C.; White, W. H. The Stereochemistry of Bis(α,α' -diimine)-copper(I) Complexes: the Crystal and Molecular Structures of Bis(2,9-dimethyl-1,10-phenanthroline)-copper(I) Bromide Hydrate, Bis(4,4',6,6'-tetramethyl-2,2'-bipyridine)copper(I) Chloride Dihydrate, and Bis(2,9-dimethyl-1,10-phenanthroline)copper(I) Nitrate Dihydrate (a Re-determination). *Australian Journal of Chemistry* **1984**, *37*, 649–659.
- (S2) Penfold, T. J.; Karlsson, S.; Capano, G.; Lima, F. A.; Rittmann, J.; Reinhard, M.; Rittmann-Frank, M. H.; Braem, O.; Baranoff, E.; Abela, R.; Tavernelli, I.; Rothlisberger, U.; Milne, C. J.; Chergui, M. Solvent-induced luminescence quenching: Static and time-resolved X-ray absorption spectroscopy of a copper(I) phenanthroline complex. *Journal of Physical Chemistry A* **2013**, *117*, 4591–4601.
- (S3) Chen, L. X.; Shaw, G. B.; Novozhilova, I.; Liu, T.; Jennings, G.; Attenkofer, K.; Meyer, G. J.; Coppens, P. MLCT state structure and dynamics of a copper(I) diimine complex characterized by pump-probe x-ray and laser spectroscopies and DFT calculations. *Journal of the American Chemical Society* **2003**, *125*, 7022–7034.
- (S4) Smolentsev, G.; Soldatov, A. V.; Chen, L. X. Three-dimensional local structure of photoexcited Cu diimine complex refined by quantitative XANES analysis. *Journal of Physical Chemistry A* **2008**, *112*, 5363–5367.
- (S5) Garakyaraghi, S.; Danilov, E. O.; McCusker, C. E.; Castellano, F. N. Transient Absorption Dynamics of Sterically Congested Cu(I) MLCT Excited States. *The Journal of Physical Chemistry A* **2015**, *119*, 3181–3193.
- (S6) Iwamura, M.; Watanabe, H.; Ishii, K.; Takeuchi, S.; Tahara, T. Coherent nuclear dynamics in ultrafast photoinduced structural change of Bis(diimine)copper(I) complex. *Journal of the American Chemical Society* **2011**, *133*, 7728–7736.

- (S7) Capano, G.; Penfold, T. J.; Röthlisberger, U.; Tavernelli, I. A Vibronic Coupling Hamiltonian to Describe the Ultrafast Excited State Dynamics of a Cu(I)-Phenanthroline Complex. *CHIMIA International Journal for Chemistry* **2014**, *68*, 227–230.
- (S8) Capano, G.; Penfold, T. J.; Chergui, M.; Tavernelli, I. Photophysics of a copper phenanthroline elucidated by trajectory and wavepacket-based quantum dynamics: a synergetic approach. *Phys. Chem. Chem. Phys.* **2017**, *19*, 19590–19600.
- (S9) Capano, G.; Rothlisberger, U.; Tavernelli, I.; Penfold, T. J. Theoretical Rationalization of the Emission Properties of Prototypical Cu(I)-Phenanthroline Complexes. *Journal of Physical Chemistry A* **2015**, *119*, 7026–7037.
- (S10) Zgierski, M. Z. Cu(I)-2,9-dimethyl-1,10-phenanthroline: Density functional study of the structure, vibrational force-field, and excited electronic states. *The Journal of Chemical Physics* **2003**, *118*, 4045–4051.
- (S11) Moret, M.-E.; Tavernelli, I.; Chergui, M.; Rothlisberger, U. Electron localization dynamics in the triplet excited state of [Ru(bpy)₃]²⁺ in aqueous solution. *Chemistry - A European Journal* **2010**, *16*, 5889–5894.
- (S12) Gordon, K. C.; McGarvey, J. J. Time-resolved Resonance Raman Spectroscopy of bis(2,9-dimethyl-1,10-phenanthroline)copper(1+) in Solution. *Inorganic Chemistry* **1991**, *30*, 2986–2989.
- (S13) Hirshfeld, F. L. Bonded-atom fragments for describing molecular charge densities. *Theoretica Chimica Acta* **1977**, *44*, 129–138.
- (S14) Banks, J. L.; Cao, H. S.; Cho, A. E.; Damm, W.; Farid, R.; Felts, A. K.; Halgren, T. A.; Mainz, D. T.; Maple, J. R.; Murphy, R.; Philipp, D. M.; Repasky, M. P.; Zhang, L. Y.; Berne, B. J.; Friesner, R. A.; Gallicchio, E.; Levy, R. M. Integrated Modeling Program,

- Applied Chemical Theory (IMPACT). *Journal of Computational Chemistry* **2005**, *26*, 1752.
- (S15) Bowers, K. J.; Chow, D. E.; Xu, H.; Dror, R. O.; Eastwood, M. P.; Gregersen, B. A.; Klepeis, J. L.; Kolossvary, I.; Moraes, M. A.; Sacerdoti, F. D.; Salmon, J. K.; Shan, Y.; Shaw, D. E. Scalable Algorithms for Molecular Dynamics Simulations on Commodity Clusters. SC '06: Proceedings of the 2006 ACM/IEEE Conference on Supercomputing. 2006; pp 43–43.
- (S16) Abedi, M.; Levi, G.; Zederkof, D. B.; Henriksen, N. E.; Pápai, M.; Møller, K. B. Excited-state solvation structure of transition metal complexes from molecular dynamics simulations and assessment of partial atomic charge methods. *Phys. Chem. Chem. Phys.* **2019**, *21*, 4082–4095.
- (S17) Guardia, E.; Pinzón, R.; Casulleras, J.; Orozco, M.; Luque, F. J. Comparison of different three-site interaction potentials for liquid acetonitrile. *Molecular Simulation* **2001**, *26*, 287.
- (S18) Larsen, A. H.; Vanin, M.; Mortensen, J. J.; Thygesen, K. S.; Jacobsen, K. W. Localized atomic basis set in the projector augmented wave method. *Phys. Rev. B* **2009**, *80*, 195112.
- (S19) Andersen, H. C. Rattle: A "velocity" version of the shake algorithm for molecular dynamics calculations. *Journal of Computational Physics* **1983**, *52*, 24.
- (S20) Van Gunsteren, W. F.; Karplus, M. A method for constrained energy minimization of macromolecules. *Journal of Computational Chemistry* **1980**, *1*, 266–274.
- (S21) Ryckaert, J. P.; Ciccotti, G.; Berendsen, H. J. C. Numerical integration of the cartesian equations of motion of a system with constraints: molecular dynamics of n-alkanes. *Journal of Computational Physics* **1977**, *23*, 327–341.

- (S22) Ciccotti, G.; Ryckaert, J. P. Molecular dynamics simulation of rigid molecules. *Computer Physics Reports* **1986**, *4*, 346–392.
- (S23) Ciccotti, G.; Ferrario, M.; Ryckaert, J.-P. Molecular dynamics of rigid systems in cartesian coordinates A general formulation. *Molecular Physics* **1982**, *47*, 1253–1264.
- (S24) Vanden-Eijnden, E.; Ciccotti, G. Second-order integrators for Langevin equations with holonomic constraints. *Chemical Physics Letters* **2006**, *429*, 310–316.